Hysteretic capacitance-voltage characteristics of self-assembled quantum dots far from equilibrium with their environment

L. Schnorr, O. Khoukhi, L. Berg, and T. Heinzel*
Solid State Physics Laboratory, Heinrich-Heine-Universität Düsseldorf, 40204 Düsseldorf, Germany

C. Rothfuchs-Engels,† S. Scholz, A. Ludwig, and A. D. Wieck
Lehrstuhl für Angewandte Festkörperphysik, Ruhr-Universität Bochum, 44780 Bochum, Germany

(Received 22 September 2021; revised 15 November 2021; accepted 16 November 2021; published 29 November 2021)

Capacitance-voltage measurements on self-assembled quantum dot layers exposed to strong electric fields and with large distances to the reservoirs show a marked hysteretic behavior. It is shown that at low temperatures this hysteresis can be explained quantitatively in terms of state-dependent capture and emission rates that are obtained by a rate equation model, applied to the measured capacitance transients. The occupation dynamics and the steady-state configuration can be extracted from these data via a Markov chain model.

DOI: 10.1103/PhysRevB.104.205310

I. INTRODUCTION

Self-assembled quantum dots (SAQDs) are quasi-zero-dimensional semiconductor islands embedded in a crystalline semiconductor host [1,2]. Due to the electronic band offsets, they are capable of capturing, storing, and re-emitting electrons or holes, respectively. SAQDs have been of great scientific interest over the past three decades due to their versatility for fundamental research [3–6] as well as because of their application potential [7]. SAQDs are used routinely in semiconductor optoelectronics, in particular in quantum dot lasers [8,9], single photon sources [10], and light-emitting diodes [11]. Regarding all-electronic applications like memory cells [12–14] or memristors [15], it is well known that the charging/discharging dynamics of SAQDs can generate hysteretic behavior as a function of a bias voltage [16–22], detectable, for example, in the capacitance of the structure [21–24] or in the conductance of a nearby conductive channel, on which the SAQDs act as a floating gate [14,18–20,22,25–29]. Charging/discharging times of 600 ps have been reported [30], while the storage time depended strongly on the temperature and can reach values of 10^4 s at a temperature of 180 K [13]. The markedness of the hysteresis depends, in general, on the modifications of the potential landscape accompanied by the electron transfer [28,31]. For several experiments, these modifications were described qualitatively and with high plausibility [18,19,21–24]. However, to understand these hysteretic effects in more detail, a quantitative description is desirable. In particular, it is important to be able to determine the capture and emission rates of the SAQD states as a function of the external parameters. Such information can be useful not only to explain certain phenomena in more detail, like the inversion of the hysteresis orientation above a threshold bias [32] or nontrivial shapes of hysteresis loops [20], but also to improve characteristic values, for example, the limits for ultrafast charging of SAQDs [33], relevant for single-photon sources.

Here, we present an experimental concept which allows the determination of the bias voltage-dependent (and temperature-dependent) capture and emission rates of the SAQD states that take part in the hysteresis. The SAQDs are in states far from equilibrium with the environment due to the strong electric field and large distances to reservoirs prevent corresponding elastic electron transfers. Such a layout is typical for memory devices as well as for optoelectronic applications. Deep level transient spectroscopy (DLTS, [34]), a well-established technique in the field [35–44], is used in its version of *Lock in–DLTS* [45], as an excellent compromise between high-energy resolution and acceptable measurement times. A rate equation model allows to extract the electron transfer rates of the participating states from the measured capacitance transients. From these rates, the average electron occupation numbers of the SAQDs as a function of time are determined. They not only provide an explanation in terms of the corresponding depletion region width z_d, but also describe the measured hysteresis loop quite well and allow the prediction of the steady-state configuration in the limit of negligible voltage sweep rates.

In Sec. II, the sample and the experimental methods are described. Section III reports the DLTS measurements, which are analyzed within the rate equation model in Sec. IV. These results are used in Sec. V for the modeling and explanation of the capacitance voltage hysteresis, and in Sec. VI for calculating the steady state. The paper concludes with a summary and an outlook (Sec. VII).

II. EXPERIMENTAL SETUP AND MEASUREMENT TECHNIQUES

The sample structure and the measurement technique were described in detail elsewhere [43,44]. In brief, we use a

*thomas.heinzel@hhu.de
†Present address: DESY, Notkestrasse 85, 22607 Hamburg, Germany.

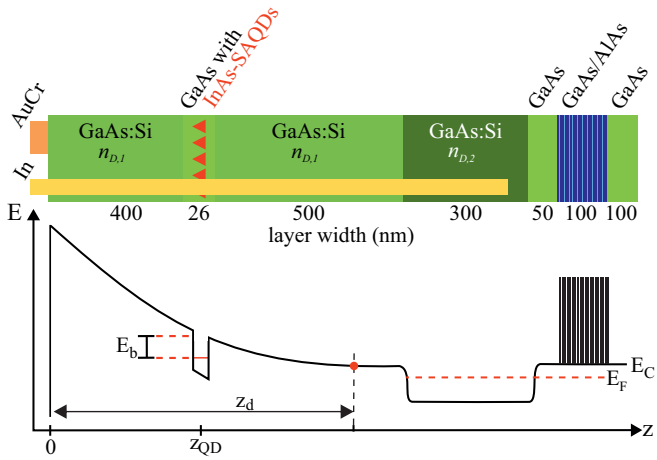

FIG. 1. Top: Cross-sectional schematic view of the sample layout. The SAQD layer is indicated by the red triangles. The back electrode is accessed via an alloyed In contact, and the top gate is formed by a Cr/Au electrode. Silicon doping densities are indicated by $n_{D,1}$ and $n_{D,2}$. Bottom: Schematic band diagram for the case of a negative voltage applied to the top gate with respect to the grounded back electrode, including our conventions for the quantities of relevance. The width of the depletion layer is denoted by z_d.

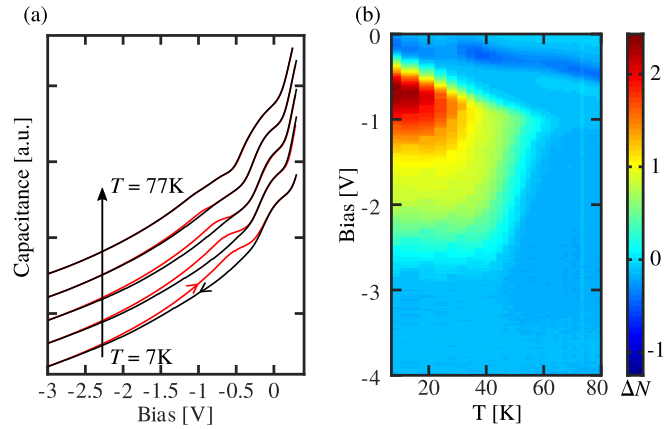

FIG. 2. (a) Capacitance-voltage hysteresis as a function of temperature with red and black lines corresponding to the up- and down-sweeps, respectively. The temperature values are (from bottom to top) $T = 7\,\mathrm{K}$, $22\,\mathrm{K}$, $33\,\mathrm{K}$, $52\,\mathrm{K}$, and $77\,\mathrm{K}$. Adjacent traces are offset vertically for clarity. (b) Difference of the number of electrons stored per SAQD between the up- and down-sweep as a function of the bias voltage and temperature.

GaAs/AlAs heterostructure as a model system, grown by molecular beam epitaxy, with a SAQD layer 500 nm above a Si^+-doped back contact and 426 nm below the sample surface, see Fig. 1(a). The InAs SAQDs have a sheet number density of $n_{QD} = 10^{14}\,\mathrm{m}^{-2}$ and are embedded in a 26-nm layer of undoped GaAs. Bias voltages can be applied between a square Cr/Au top electrode (edge length 0.3 mm) and the back electrode, which is accessed via an alloyed In contact. The densities of the Si doping in the spacer layers are $n_{D,1} = 6.02\times10^{21}\ \mathrm{m}^{-3}$ and $n_{D,2} = 2\times10^{24}\ \mathrm{m}^{-3}$. The active sample area covers approximately 9×10^6 quantum dots.

The sample is inserted into a liquid helium cryostat with a temperature range from 3 K to 300 K. DC bias voltages are applied to the top gate with respect to the back contact, kept at virtual ground via a HF2TA transimpedance amplifier ($Z = 1\,\mathrm{k}\Omega$) from Zurich Instruments, the output of which is fed into a Zurich Instruments HF2LI lock in amplifier. The voltage pulses are generated using a Keithley Model 3390 arbitrary waveform generator with a transition time of 100 ns and are superimposed to the AC test voltage generated by the lock in amplifier. Thus, the output current obtained at a phase shift of $\pi/2$ with respect to the input AC voltage detects the differential capacitance of the sample.

III. EXPERIMENTAL RESULTS

A. Capacitance-voltage measurements and their temperature dependence

Multiple capacitance-voltage sweeps between $V = -4\,\mathrm{V}$ and $V = +0.3\,\mathrm{V}$ were recorded at various temperatures between $T = 7\,\mathrm{K}$ and room temperature. For each temperature both the up- and down-sweeps were measured. The bias voltage step size was $\Delta V = 12.5\,\mathrm{mV}$ with a waiting time of $\Delta t = 0.85\,\mathrm{s}$ and the capacitance was measured via a test signal with an amplitude of $V_{ac} = 10\,\mathrm{mV}$ and a frequency of $f_{ac} = 10.44\,\mathrm{MHz}$. The lock in time constant was set to $\tau = 20.33\,\mathrm{ms}$. A selection of these traces is shown in Fig. 2(a).

As the bias voltage is increased from $V = -4\,\mathrm{V}$ to $V = +0.3\,\mathrm{V}$ at $T = 7\,\mathrm{K}$ [lower-most trace in Fig. 2(a)], two peaks can be observed on top of the smooth voltage dependence expected for a Schottky diode capacitance, one at $V \approx -0.6\,\mathrm{V}$ and a second one at $V = 0\,\mathrm{V}$. In the successive down-sweep, however, only the peak at $V = 0\,\mathrm{V}$ is observed, while the second one is absent. A similar behavior was reported in earlier work [13,24,46]. This hysteretic behavior is the main focus of the present work.

As the temperature is increased, both features shift towards lower bias voltages. The hysteretic peak becomes weaker until it vanishes at about $T = 60\,\mathrm{K}$. The nonhysteretic peak, however, becomes more pronounced as the temperature is increased up to $T \approx 150\,\mathrm{K}$ above which its shape and position remain essentially unchanged (not shown).

In Fig. 2(b), the difference ΔN in the number of electrons stored per SAQD between the up- and down-sweeps is shown as a function of the bias voltage and the temperature, see Sec. V for details. The maximum hysteresis opening thus corresponds to a charge difference of more than two electrons per SAQD at low temperatures. Qualitatively, its origin can be described as follows [24]. At sufficiently negative bias voltages V the SAQDs are empty. As V is increased, the width z_d of the space charge layer decreases according to $z_d = \sqrt{\frac{2\epsilon\epsilon_0}{eN_D}(V_{bi} - V)}$, where V_{bi} is the built-in voltage and e denotes the elementary charge. This leads to an increase of the capacitance according to $C = \epsilon\epsilon_0 A/z_d$, where A denotes the area underneath the top gate, which causes the smooth increase of C with V. Above a threshold voltage, electrons are captured at a significant rate by the SAQDs, leading to an average electron number N per SAQD. This causes an increase of z_d since these electrons have to be compensated

by additional positively charged donor ions [46]

$$z_d(N) = \sqrt{\frac{2}{en_D}[\epsilon\epsilon_0(V_{bi} - V) + Nen_{QD}z_{QD}]}. \quad (1)$$

As a consequence, the capacitance decreases to $C = \epsilon\epsilon_0 A/z_d(N)$ when the steady state is reached. During our up-sweeps and in the hysteresis interval, however, the sweep rate is comparable to or larger than the smallest charge transfer rate, and the steady state has not yet been reached. Consequently, a larger capacitance as compared to the steady-state value is measured. Likewise, in a down-sweep, the measured capacitance can be smaller than its steady-state value. Therefore, one expects to observe characteristic capacitance transients in response to voltage steps with positive (negative) sign for negative (positive) voltage steps and with time constants that depend on the capture and emission rates of the participating SAQD states. As we will show below, the relation between the time constants of the transients and the state-dependent electron transfer rates is nontrivial but explains the hysteresis in quantitative terms.

B. Lock in: DLTS measurements

We determine the electron transfer rates from capacitance transients of the sample in response to abrupt voltage steps. The transients are characterized by lock in–DLTS measurements at four selected temperatures, namely at $T = 7\,\mathrm{K}$, 16 K, 41 K, and 77 K. Measurement voltages $V_m \in [-3.0\,\mathrm{V}, 0\,\mathrm{V}]$ were applied after preparation voltages V_p. Each voltage was applied for a time interval $t_p = t_m = 498\,\mathrm{ms}$. Measurements were recorded for combinations of V_p and V_m over the measurement interval with a voltage step size of $\Delta V = 40\,\mathrm{mV}$. Afterwards, the lock in signal $S(V_p, V_m)$ was calculated according to

$$S(V_p, V_m) = \sum_{i=1}^{N_t/2} C(t_i, V_p, V_m) - \sum_{i=N_t/2+1}^{N_t} C(t_i, V_p, V_m), \quad (2)$$

where N_t is the number of time samples in the recorded transient. Thus, the lock in signal represents the difference of the areas in the first and the second half of the transient. It approaches zero for time constants much smaller or much larger than the measurement window and shows a maximum for a time constant of ≈40% of the evaluated recording time [44]. The results are shown in Fig. 3.

At $T = 7\,\mathrm{K}$, three clearly separated negative emission peaks can be observed at $V_p > -0.5\,\mathrm{V}$ for $V_m \approx -2.55\,\mathrm{V}$, $V_m \approx -1.2\,\mathrm{V}$, and $V_m \approx -0.4\,\mathrm{V}$. All emission peaks are approximately symmetric with respect to V_m. For $V_p < -0.5\,\mathrm{V}$, electron capture can be observed via a positive lock in–DLTS signal at $V_m \approx (-0.4 \pm 0.1)\,\mathrm{V}$. Outside of the transition region from electron emission to capture at $V_p \approx -0.5\,\mathrm{V}$ the emission peaks do not exhibit any dependence on V_p. The capture peak, however, shows a step-like dependence on V_p on its border towards smaller V_m with two steps occurring at approximately $V_p = -1.25\,\mathrm{V}$ and $V_p = -2.4\,\mathrm{V}$.

At $T = 16\,\mathrm{K}$, the features remain qualitatively unchanged, with the capture and emission signals at the largest V_m values shifting towards smaller V_m. The transition region between the capture and emission regimes has decreased to $V_p \approx -0.6\,\mathrm{V}$.

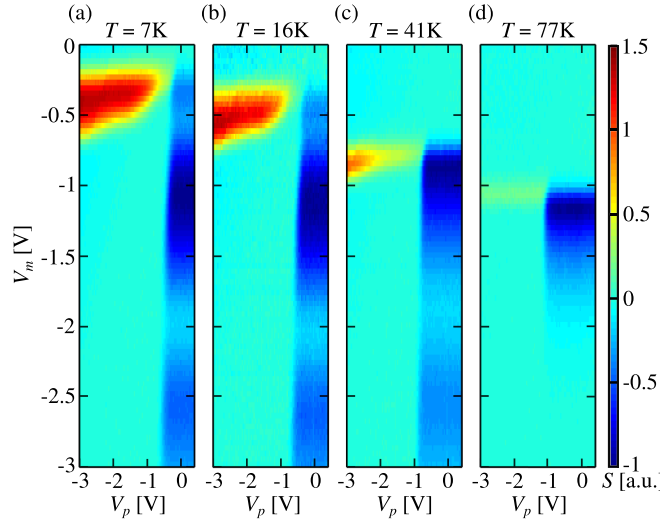

FIG. 3. Lock in–DLTS measurements at $T = 7$ K, 16 K, 41 K, and 77 K (a)–(d). The colorscale value of each spectrum is scaled to −1 at its respective minimum.

At $T = 41\,\mathrm{K}$, however, the changes are more pronounced: only two emission peaks can be observed, a large one that is asymmetric with respect to V_m as well as an approximately symmetric one centered at $V_m \approx -2.55\,\mathrm{V}$, separated by a minimum at $V_m \approx -0.9\,\mathrm{V}$. The capture signal is significantly weaker compared to those at lower temperatures and now covers the interval $V_m \in [-1\,\mathrm{V}, -0.75\,\mathrm{V}]$. A slight dependence of its low-voltage edge on V_p can still be observed, but the resolution is too small to identify the steps here. The transition region between the capture and emission regimes has shifted downwards to $V_p \approx -0.9\,\mathrm{V}$.

Only one asymmetrical emission signal can be observed at $T = 77\,\mathrm{K}$, which has its minimum at $V_m \approx -1.2\,\mathrm{V}$. A relatively weak capture signal at $V_m \approx -1.05\,\mathrm{V}$ can still be detected. Neither the capture nor the emission peaks show a V_p dependence outside the transition region that has now shifted to $V_p \approx -1\,\mathrm{V}$.

Thus, a monotonous behavior of the temperature dependence is observed: as the T increases, the capture signal becomes less pronounced compared to the strongest respective emission peak, while its position moves in the direction of smaller V_m. The transition region between electron capture and emission shifts towards smaller V_p as T is increased. The fine-structure of both the capture and emission signals smear out as T increases. Furthermore, no emission signals can be observed at measurement voltages larger than the upper boundary of the capture structure on the V_m axis.

In the following, we restrict ourselves to an analysis of the situation at the lowest temperature, where the richest structure is observed and the emission occurs by elastic tunneling only. A quantitative discussion of the behavior at larger temperatures, where thermally activated processes are significant, is beyond our scope here and will be provided elsewhere.

IV. RATE EQUATION MODEL

To analyze quantitatively the observed lock in–DLTS signals taken at $T = 7\,\mathrm{K}$, we proceed by modeling the charge

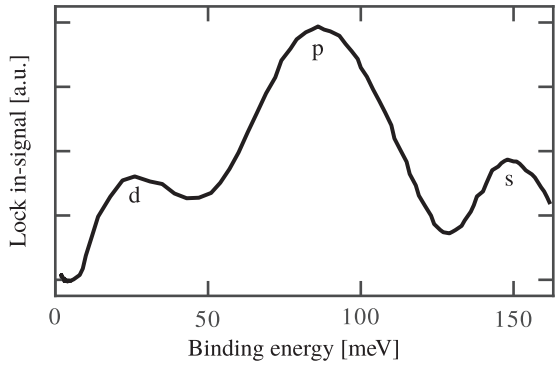

FIG. 4. Energy spectrum obtained from the emission features observed at $T = 7\,\mathrm{K}$, calculated via Eq. (3).

transfer dynamics by a system of coupled differential equations [47].

A. Rate equations for the electron transfer dynamics

Based on previous measurements on the same sample [43] we attribute the emission feature observed at $V_m \approx -2.6\,\mathrm{V}$ at $T = 7\,\mathrm{K}$ to electron emission from the s-states.

In analogy to the analysis described in Ref. [43], the energy spectrum can be calculated from the emission transients, but now at temperatures where elastic tunneling is dominant. Via the relationship derived by Korol *et al.* [48], the time constant of the capacitance transient is given by

$$\tau = \frac{4\sqrt{2m^* E_b}}{eF} \exp\left(\frac{4}{3}\frac{\sqrt{2m^* E_b^{3/2}}}{e\hbar F}\right). \tag{3}$$

Here, E_b is the binding energy of the captured electrons (see also Fig. 1) and F denotes the electric field at the SAQD layer. The spectrum shown in Fig. 4 can be obtained by taking a line scan through the lock in–DLTS colorscale plot, Fig. 3(a), at $V_p = 0$. The voltage dependence in the obtained spectrum $S(V_m)$ can be converted into an electric field-dependent spectrum $S(F)$ via the voltage-dependent band structure of the sample as obtained from a one-dimensional Poisson-Schrödinger solver [49]. This electric field dependence is then converted into energy and presented in Fig. 4 by solving numerically Eq. (3) for the binding energy E_b with $\tau = \text{const.} = 0.398 \cdot t_m = 198\,\mathrm{ms}$, fixed by our transient recording time and the rate window of lock in signal.

The large energy spacing of $\approx$60 meV between the peaks, as well as their relative magnitude indicate that they originate from the s (smallest V_m), p, and d (largest V_m) states. Sublevels like s_1, s_2, p_1, and so on cannot be resolved here. We therefore assume that the step-like structure of the capture peak arises from a superposition of three different capture paths, one for the s, p, and d states each. This gives rise to the system of coupled differential equations:

$$\dot{w}_0 = -c_{0s} \cdot w_0 + r_{s0} \cdot w_s, \tag{4}$$

$$\dot{w}_s = -c_{sp} \cdot w_s + r_{ps} \cdot w_p + c_{0s} \cdot w_0 - r_{s0} \cdot w_s, \tag{5}$$

$$\dot{w}_p = +c_{sp} \cdot w_s - r_{ps} \cdot w_p + r_{dp} \cdot w_d - c_{pd} \cdot w_p, \tag{6}$$

$$\dot{w}_d = +c_{pd} \cdot w_p - r_{dp} \cdot w_d, \tag{7}$$

TABLE I. Fit parameters used to calculate the results shown in Figs. 5(b), 5(c), and 6.

x	y	$m_{xy}\,[\mathrm{V}^{-1}]$	n_{xy}	$m_{yx}\,[\mathrm{V}^{-1}]$	n_{yx}
0	s	13.53	8.63	−6.15	−14.08
s	p	16.18	7.71	−4.97	−4.16
p	d	15.68	6.35	−16.66	−2.91

where w_0 is the probability for one SAQD being empty, while w_j is the probability that state j and all states at lower energies are occupied, while all states with larger energies are empty. The capture and emission rates related to these occupation probabilities are denoted by c_{ij} and r_{ij}, $i, j \in \{0, s, p, d\}$, respectively.

The total, time-dependent occupation number per dot is then given by

$$N(t) = 2 \cdot w_s(t) + 6 \cdot w_p(t) + 12 \cdot w_d(t). \tag{8}$$

Here, the weighting factors rely on the assumption that all sublevels of each SAQD state, e.g., the p state, share the same occupancy for all times. Other reasonable assumptions are possible as well which, however, cause only marginal changes of the fit parameters discussed below (not shown).

B. Fit of the experimental transients

We proceed by fitting the rate equation model to the data using a similar approach as reported earlier [44], where the choice of the initial conditions for the differential equations and the simulation of the pulse sequences are kept the same. The individual electron transfer rates are modeled by

$$c_{xy}(V) = \exp\left(m_{xy} \cdot V + n_{xy}\right) \mathrm{s}^{-1}, \tag{9}$$

$$r_{yx}(V) = \exp\left(m_{yx} \cdot V + n_{yx}\right) \mathrm{s}^{-1}, \tag{10}$$

where $x, y \in \{0, s, p, d\}$.

The lock in signal is calculated via Eq. (2) from the total charge per dot under the assumption that red $\Delta C(t) \propto N(t)$. The constants m_{xy} and n_{xy} are the fit parameters, alongside a scaling factor that accounts for the proportionality between $N(t)$ and $\Delta C(t)$.

Equations (4) to (7) have no analytical solution. We thus solve them numerically for each iteration of the fitting process, using the RADAU solver of the SCIPY library [50] which implements a fifth-order implicit Runge-Kutta method [51].

To avoid excessive computation times, the calculated rates were limited to $\leqslant 10^3\,\mathrm{s}^{-1}$. This cutoff is justified by the recording time of $t_m = 498\,\mathrm{ms}$, which leads to a rate window of the lock in signal that is centered around $r_{\mathrm{ref}} = (0.398 \cdot t_m)^{-1} = 5.1\,\mathrm{s}^{-1}$, more than two orders of magnitude smaller.

The results of this fit algorithm are given in Table I, and the corresponding, numerically obtained lock in–DLTS signals are shown in comparison to the experimental data in Figs. 5(a) and 5(b). The resulting capture and emission rate functions are depicted in Fig. 5(c). Starting from a negative bias voltage, say $V = -3\,\mathrm{V}$, all emission rates are large as compared to the capture rates, and the SAQDs are empty in a steady state. As V is increased, the emission rates decay exponentially while significant capture sets in around $V = -1\,\mathrm{V}$. The capture rates

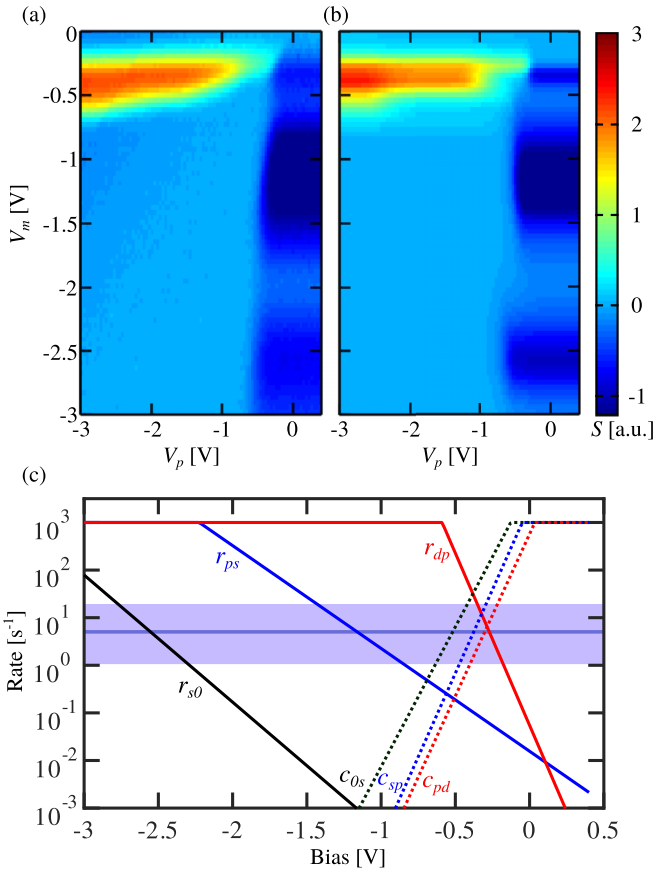

FIG. 5. (a) Measured and (b) calculated lock in–DLTS spectra for the measurement at $T = 7$ K and the voltage-dependent electron transfer rates (c), as obtained from the fit.

increase exponentially with increasing bias voltage, leading to an occupied steady state, with an occupation probability $w_j(V)$ (see below).

For the emission processes, the physical interpretation of the obtained fit parameters is straightforward: each exponential voltage dependence, parameterized by its two fit parameters, is an approximation to the general expression describing the emission dynamics, which in our case of $T = 7$ K consists of pure tunneling, Eq. (3). This approximation is valid in the voltage interval in which the resulting emission rate falls within the rate window of $r_{\mathrm{ref}} = 5.1\,\mathrm{s}^{-1}$ of our lock in–DLTS filter function. This value is denoted by the purple horizontal line in Fig. 5(c) alongside the corresponding full width at half maximum interval (indicated by the shaded area). We note that, only in this interval, our simple assumption of the respective rates as a function of the bias voltage needs to approximate the real dependence since outside this window the contribution to the measured signal is negligible. For the capture processes, we envisage a similar interpretation, but to the best of our knowledge, a model for the capture dynamics of electrons under the conditions present here is yet to be developed. It should be noted that the shape of the capture peak can only be reproduced accurately as long as $c_s > c_p > c_d$. Other scenarios lead to a qualitatively different shape (not shown). This may be indicative of the Coulomb barrier set up by the electrons already captured in the SAQDs, which (while the system remains at the same bias voltage) suppresses the capture of further electrons. Thus, the dynamics of the capture processes cannot be dominated by the tunneling barrier width in our case. This finding is in contrast to the observations by Luyken *et al.* [52] who measured larger transfer rates for higher SAQD states which they were able to explain via the increased tunneling coefficient through the smaller potential barrier. Their measurements, however, studied each SAQD state at bias voltages where the respective state was aligned with the Fermi level in the back contact and the difference between charging and discharging times was negligible to a good approximation. Our measurements, however, are carried out with the states well above the bulk Fermi level and far from equilibrium with the environment, where capture and emission rates can differ by orders of magnitudes, see Fig. 5(c).

Based on these findings, we can now interpret qualitatively the behavior at higher temperatures. The shift of the capture peak towards smaller V_m in Fig. 3 with increasing temperature is indicative of increasing capture rates. Since they become larger as V is increased, the shift of the peaks towards more negative V_m compensates the increased thermal contribution, such that the combined rate still matches our experimental rate window. The same line of arguing is applicable to the emission peaks. The measured charge transfer rates are, however, composed of the individual transfer rates in a nontrivial way [44], where the observed decay rates are never smaller than each individual charge transfer rate. This explains the asymmetry of emission peaks close to the capture peaks in the lock in–DLTS spectra since, for larger V_m than the position of the capture peaks, there will always be a capture rate larger than any emission rate that will dominate the dynamics and make it too fast to be observable.

V. APPLICATION TO THE CV HYSTERESIS

We continue by solving the system of differential Eqs. (4) to (7) using the previously determined fit parameters for the slowly varying bias voltage that was applied during the measurement of the CV hysteresis.

The system is solved numerically for two sweep cycles, each from $V = +0.3$ V to $V = -4$ V and back, with the initial condition that all SAQDs are completely filled. The bias voltage is stepped by $\Delta V = \pm 12.5$ mV (depending on the sweep direction) every $\Delta t = 0.85$ s. The calculation is considered to be finished when the solution has become independent of the initial condition.

From these simulations, the occupation probability of the SAQD states $w_j(V)$ for the down- and up-sweep is obtained, where $j \in \{0, s, p, d\}$, leading directly to a computed value for $\Delta N(V)$. Experimentally, $\Delta N(V)$ can be obtained from the measured CV hysteresis opening via the relation [46]

$$\Delta N = \frac{(\epsilon_0 \epsilon A)^2 n_D \cdot n_{QD}}{2 z_{QD}} \left(C_{\mathrm{down}}^{-2} - C_{\mathrm{up}}^{-2}\right), \tag{11}$$

where A is the gate area and $C_{\mathrm{down(up)}}$ the capacitance in a down (up)-sweep.

The corresponding computed and experimentally determined results are compared in Fig. 6(a). Reasonable agreement is found, both with respect to its magnitude and

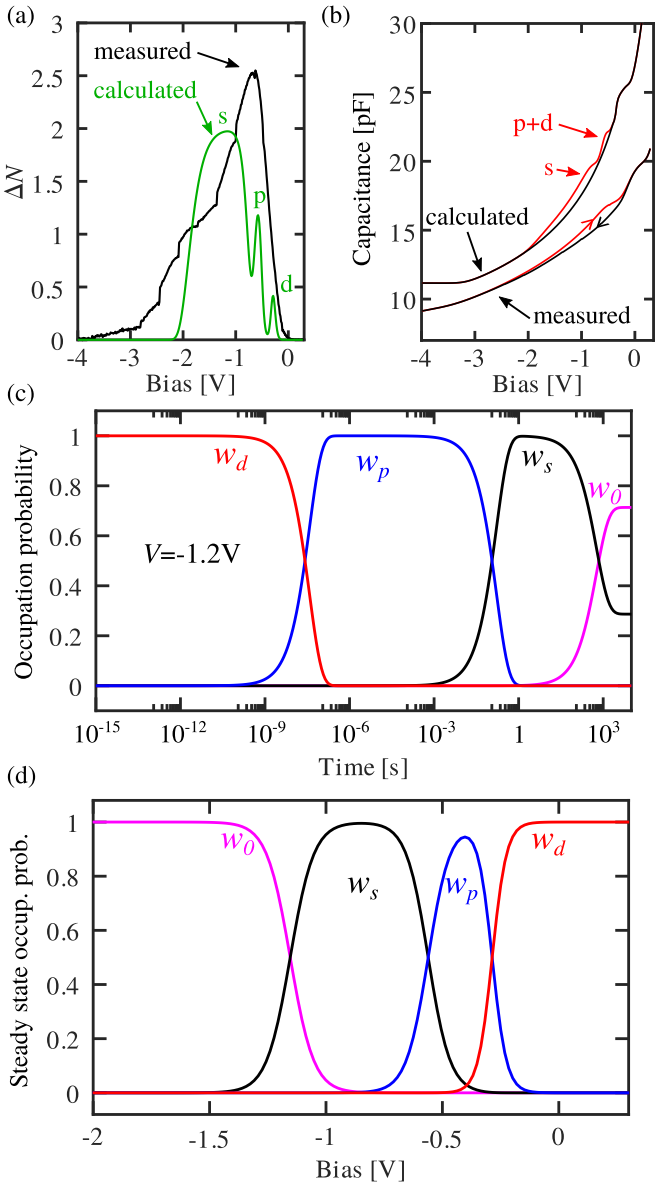

FIG. 6. Measured and calculated values for (a) ΔN, (b) measured and calculated CV hysteresis, (c) time evolution towards the steady state at $V = -1.2$ V, and the voltage dependence of the steady-state occupancy at (d) $T = 7$ K.

its position along the bias voltage axis. In the calculation the contributions of the individual charge states can be resolved, whereas in the measurement, such an attribution is not possible. The assignment of the three features in the calculation to the individual charge states is obtained by setting the respective contribution of one state to zero and checking which feature vanishes. It is obvious that the *s* states form the largest contribution to the hysteresis, which seems plausible since their electron transfer rates are the smallest ones, they are thus affected most strongly by the varying bias voltage. For the *p* states, a small contribution is visible, while the participation of the *d* states, however, is close to be negligible since they can adapt sufficiently rapidly to the changed bias voltage.

To reproduce the CV characteristics of the down-sweep numerically, the band structure of the sample is solved in a first step, using a one-dimensional Poisson and Schrödinger solver [49]. A doping density of $n_{D,1} = 6.02\times10^{21}\,\mathrm{m}^{-3}$ as obtained from a $C^{-2}(V)$ analysis of the measured down-sweep was used, and the SAQD layer was simulated by a 21-nm layer of InGaAs with a constant charge density. The result of this simulation for $T = 7$ K is shown in Fig. 6(b) (upper black trace). It can be seen that the nonhysteretic shoulder at $V \approx 0$ is reproduced simply by the different layered materials. By rearranging Eq. (11) we can obtain the capacitance of the up-sweep from the calculated down-sweep and the simulated charge difference between the sweeps. The result is shown in Fig. 6(b) (upper red curve). Good agreement with the measurement [lower traces in Fig. 6(b)] can be observed regarding the boundaries of the hysteresis on the voltage axis. Two separate peaks can be observed for the *s*- and *p*-state contributions in the simulation, which cannot be resolved in the measurement. The hysteresis due to the *d* states is completely invisible in the CV curve.

Thus, by the analysis presented above, the qualitative picture developed in Sec. III A can be quantified and interpreted in terms of the weight by which individual SAQD states contribute to the hysteresis via their capture and emission rates. The good agreement between the measurements and the model furthermore implies that changes of the electron transfer rates by variation of the occupation numbers of the SAQDs are of minor importance, albeit this effect may explain the remaining deviations between the model and the experiment. These effects are hard to quantify since this would require unreasonably many fit parameters in our model, or maybe even a three-dimensional treatment of the SAQD potential as a function or their occupation, which is beyond our present scope.

Under the assumption that the average charge density in the SAQD layer is small compared to the doping density, the maximum, normalized opening of the hysteresis trace can be approximated as [46] $\Delta C/C_s = Ne n_{QD} z_{QD}/2\epsilon\epsilon_0(V_{bi} - V)$. Hence, the opening of this type of hysteresis can be maximized by increasing n_{QD} or z_{QD} to their upper limits and can be suppressed by corresponding minimizations.

As the temperature is increased, the transfer rates increase as well and the SAQDs come closer to their steady state during the time window $\Delta t = 0.85$ s at each voltage. Thus, the hysteresis decreases and vanishes for our parameters at $T \approx 60$ K, see Fig. 2(b). While for the model presented here, there is no analytical expression for the observable capacitance transient as a function of the individual rates, it is reasonable to assume that the combined rate can never be slower than any individual rate. Hence, the maximum sweep rate where no hysteresis can be observed can be estimated from our model by taking the slowest individual electron transfer rate for the *s* state at $V \approx -1.2$ V, i.e., $r_{\min} \approx 10^{-3}\,\mathrm{s}^{-1}$ for $T = 7$ K, as the limiting factor.

VI. CALCULATION OF THE STEADY-STATE CONFIGURATION

The experimentally determined electron transfer rates can be used as input for a continuous time [53] Markov chain [54] model, with the goal to obtain the steady-state configuration, which may be inaccessible experimentally, for example, due

to the required slow voltage sweep rates. In this picture, the states of the Markov chain correspond to the charge states $(0, s, p, d)$ of the SAQDs in that particular order, and we can therefore define the corresponding transition rate matrix [53] for each bias voltage as

$$Q = \begin{pmatrix} -c_{0s} & c_{0s} & 0 & 0 \\ r_{s0} & -(r_{s0} + c_{sp}) & c_{sp} & 0 \\ 0 & r_{ps} & -(r_{ps} + c_{pd}) & c_{pd} \\ 0 & 0 & r_{dp} & -r_{dp} \end{pmatrix}, \quad (12)$$

from which the occupation numbers follow via

$$P(t) = \exp(Qt), \quad (13)$$

and thus the steady-state configuration follows according to

$$P = \lim_{t\to\infty} \exp(Qt), \quad (14)$$

which was evaluated numerically using GNU OCTAVE [55].

Figure 6(c) shows, as an example, the time evolution of the system from an initial state where all SAQD states are occupied, i.e., at $V = 0$, towards its steady-state configuration at $V = -1.2$ V where the s states have equal capture and emission rates. It can be seen that the d states have a lifetime of the order of microseconds while the s states decay on the order of seconds. In general, we observed a convergence towards the steady state after, at most, 6000 s for the voltage range studied here. Calculation examples for further scenarios are given in the Supplemental Material [56].

Thus, to measure a steady-state CV of our system at $T = 7$ K, one would have to wait at least $t = 6000$ s between each voltage step which makes such an experiment impractical. Therefore, the numerical determination of the steady-state occupation probability represents a valid alternative. Here, the voltage-dependent steady-state configuration was calculated by approximating the limit in Eq. (14) by setting $t = 10^7$ s. In the steady-state configuration the rows of P are identical and the columns correspond to the occupation probability of the corresponding SAQD state. For our system this result is shown in Fig. 6(d). It can be seen that for $V < 1.5$ V the SAQDs are empty. For $V < -0.9$ V only the s states contribute to the filling factor whereas for $V < -0.5$ V both the s and the p states are contributing. Only for $V > -0.5$ V do the d states begin to be filled with electrons.

VII. SUMMARY AND OUTLOOK

The hysteretic capacitance-voltage characteristics of self-assembled quantum dot layers with large distances to reservoirs and in strong electric fields was measured and the charge transfer dynamics was analyzed within a rate equation model. It has emerged how the hysteresis is determined by the capture and emission rates of the SAQD states, which were obtained via lock in–DLTS. Reasonable quantitative agreement of the experimentally observed and calculated hysteresis traces as well as of the measured and calculated electron occupation numbers is found for all temperatures. The evolution of these rates as a function of the bias voltage supports an intuitive picture for the origin of the hysteresis, namely a time-dependent change of the width of the depletion region that forms between the top gate and the back electrode. Changes of the electron transfer rates by the local potential close to the SAQDs, on the other hand, appear to be of minor relevance in our system, but may be responsible for the residual deviations of the model to the experimental data. It has also been shown how these rates can be used to model the steady-state configuration, which may be inaccessible experimentally. Furthermore, the state-resolved capture rates have been measured, revealing that lower-lying states have larger capture rates, as one might expect from energetic considerations. The developed methodology is quite universal and can be applied to a variety of related scenarios, like storage of holes in SAQDs, different material systems, or the effect of the SAQD occupation number on the conductance of a nearby electron gas, as long as the relevant transfer rates lie within the experimentally accessible rate window. Hopefully, our studies inspire future work towards a better understanding of such systems, in particular regarding the electron capture process.

ACKNOWLEDGMENTS

Computational support and infrastructure was provided by the "Centre for Information and Media Technology" (ZIM) at the University of Düsseldorf (Germany). C.R., S.E.S., A.D.W., and A.L. gratefully acknowledge support of TRR 160/2-Project B04, DFG 383065199, and the DFH/UFA CDFA-05-06.

[1] D. Leonard, M. Krishnamurthy, C. M. Reaves, S. P. Denbaars, and P. M. Petroff, Appl. Phys. Lett. **63**, 3203 (1993).
[2] P. M. Petroff, A. Lorke, and A. Imamoglu, Phys. Today **54**, 46 (2001).
[3] P. Michler, A. Kiraz, C. Becher, W. V. Schoenfeld, P. M. Petroff, L. Zhang, E. Hu, and A. Imamoglu, Science **290**, 2282 (2000).
[4] M. Kroutvar, Y. Ducommun, D. Heiss, M. Bichler, D. Schuh, G. Abstreiter, and J. J. Finley, Nature (London) **432**, 81 (2004).
[5] C. L. Salter, R. M. Stevenson, I. Farrer, C. Nicoll, D. A. Ritchie, and A. J. Shields, Nature (London) **465**, 594 (2010).
[6] A. Faraon, A. Majumdar, D. Englund, E. Kim, M. Bajcsy, and J. Vuckovic, New J. Phys. **13**, 055025 (2011).
[7] D. J. Mowbray and M. S. Skolnick, J. Phys. D: Appl. Phys. **38**, 2059 (2005).
[8] V. M. Ustinov, N. A. Maleev, A. E. Zhukov, A. R. Kovsh, A. Y. Egorov, A. V. Lunev, B. V. Volovik, I. L. Krestnikov, Y. G. Musikhin, N. A. Bert, P. S. Kopev, and Z. I. Alferov, Appl. Phys. Lett. **74**, 2815 (1999).
[9] E. U. Rafailov, M. A. Cataluna, and W. Sibbett, Nat. Photon. **1**, 395 (2007).
[10] S. Buckley, K. Rivoire, and J. Vučković, Rep. Prog. Phys. **75**, 126503 (2012).

[11] I. L. Krestnikov, N. A. Maleev, A. V. Sakharov, A. R. Kovsh, A. E. Zhukov, A. F. Tsatsulnikov, V. M. Ustinov, Z. I. Alferov, N. N. Ledentsov, D. Bimberg, and J. A. Lott, Semicond. Sci. Technol. **16**, 844 (2001).
[12] M. Geller, A. Marent, T. Nowozin, and D. Bimberg, J. Phys. Cond. Mat. **20**, 454202 (2008).
[13] T. Nowozin, A. Marent, M. Geller, D. Bimberg, N. Akcay, and N. Öncan, Appl. Phys. Lett. **94**, 042108 (2009).
[14] A. Marent, T. Nowozin, M. Geller, and D. Bimberg, Semicond. Sci. Technol. **26**, 014026 (2011).
[15] P. Maier, F. Hartmann, M. Emmerling, C. Schneider, M. Kamp, S. Hofling, and L. Worschech, Phys. Rev. Appl. **5**, 054011 (2016).
[16] K. Koike, K. Saitoh, S. Li, S. Sasa, M. Inoue, and M. Yanoa, Appl. Phys. Lett. **76**, 1464 (2000).
[17] N. Ooike, J. Motohisa, and T. Fukui, Jpn. J. Appl. Phys. **46**, 4344 (2007).
[18] C. R. Muller, L. Worschech, J. Heinrich, S. Höfling, and A. Forchel, Appl. Phys. Lett. **93**, 063502 (2008).
[19] A. Marent, T. Nowozin, J. Gelze, F. Luckert, and D. Bimberg, Appl. Phys. Lett. **95**, 242114 (2009).
[20] P. Maier, F. Hartmann, M. Emmerling, C. Schneider, S. Höfling, M. Kamp, and L. Worschech, Appl. Phys. Lett. **105**, 053502 (2014).
[21] D. Nataraj, N. Ooike, J. Motohisa, and T. Fukui, Appl. Phys. Lett. **87**, 193103 (2005).
[22] E. S. Kannan, G.-H. Kim, and D. A. Ritchie, Appl. Phys. Lett. **95**, 143506 (2009).
[23] M. Geller, A. Marent, T. Nowozin, D. Bimberg, N. Akçay, and N. Öncan, Appl. Phys. Lett. **92**, 092108 (2008).
[24] A. Gubanov, A. Schramm, V. Polojärvi, and M. Guina, J. Phys. D: Appl. Phys. **46**, 325102 (2013).
[25] C. Balocco, A. M. Song, and M. Missous, Appl. Phys. Lett. **85**, 5911 (2004).
[26] B. Marquardt, M. Geller, A. Lorke, D. Reuter, and A. D. Wieck, Appl. Phys. Lett. **95**, 022113 (2009).
[27] M. Geller, B. Marquardt, A. Lorke, D. Reuter, and A. D. Wieck, Nanoscale Res. Lett. **5**, 829 (2010).
[28] Y.-A. Liao, Y.-K. Chao, S.-W. Chang, W.-H. Chang, J.-I. Chyi, and S.-Y. Lin, Appl. Phys. Lett. **103**, 143502 (2013).
[29] T. Nowozin, A. Beckel, D. Bimberg, A. A. Lorke, and M. Geller, Appl. Phys. Lett. **104**, 053111 (2014).
[30] J. Nannen, W. Quitsch, S. Eliasson, T. Kummell, and G. Bacher, Phys. Rev. B **85**, 035325 (2012).
[31] H. Lu, F. Guo, B. Zhang, and W. Ning, Micro & Nano Lett. **11**, 623 (2016).
[32] C. R. Muller, L. Worschech, and A. Forchel, Phys. Rev. B **79**, 205307 (2009).
[33] J. Nannen, T. Kummell, M. Bartsch, K. Brunner, and G. Bacher, Appl. Phys. Lett. **97**, 173108 (2010).
[34] D. V. Lang, J. Appl. Phys. **45**, 3023 (1974).
[35] S. Anand, N. Carlsson, M.-E. Pistol, L. Samuelson, and W. Seiffert, Appl. Phys. Lett. **67**, 3016 (1995).
[36] C. M. A. Kapteyn, F. Heinrichsdorff, O. Stier, R. Heitz, M. Grundmann, N. D. Zakharov, D. Bimberg, and P. Werner, Phys. Rev. B **60**, 14265 (1999).
[37] S. W. Lin, C. Balocco, M. Missous, A. R. Peaker, and A. M. Song, Phys. Rev. B **72**, 165302 (2005).
[38] S. Schulz, A. Schramm, C. Heyn, and W. Hansen, Phys. Rev. B **74**, 033311 (2006).
[39] M. Geller, E. Stock, C. Kapteyn, R. L. Sellin, and D. Bimberg, Phys. Rev. B **73**, 205331 (2006).
[40] O. Engström, M. Kaniewska, M. Kaczmarcyk, and W. Jung, Appl. Phys. Lett. **91**, 133117 (2007).
[41] A. Schramm, S. Schulz, T. Zander, C. Heyn, and W. Hansen, Phys. Rev. B **80**, 155316 (2009).
[42] T. Nowozin, L. Bonato, A. Högner, A. Wiengarten, D. Bimberg, W.-H. Lin, S.-Y. Lin, C. J. Reyner, B. L. Liang, and D. L. Huffaker, Appl. Phys. Lett. **102**, 052115 (2013).
[43] L. Schnorr, T. Heinzel, S. Scholz, A. Ludwig, and A. D. Wieck, J. Appl. Phys. **124**, 104301 (2018).
[44] L. Schnorr, J. Labes, L. Kurten, T. Heinzel, C. Rothfuchs-Engels, S. Scholz, A. Ludwig, and A. D. Wieck, Phys. Rev. B **104**, 035303 (2021).
[45] D. S. Day, M. Y. Tsai, B. G. Streetman, and D. V. Lang, J. Appl. Phys. **50**, 5093 (1979).
[46] S. Schulz, Ph.D. Thesis, Hamburg University (2005).
[47] V. Korobov and V. Ochkov, *Chemical Kinetics with Mathcad and Maple* (Springer, Vienna, 2011).
[48] E. N. Korol, Ukr. Phys. J. **18**, 1890 (1973).
[49] G. Snider, 1D Poisson-Schrodinger solver (2017), https://www3.nd.edu/~gsnider/, Accessed on Sep. 15th, 2017.
[50] P. Virtanen, R. Gommers, T. E. Oliphant, M. Haberland, T. Reddy, D. Cournapeau, E. Burovski, P. Peterson, W. Weckesser, J. Bright, S. J. van der Walt, M. Brett, J. Wilson, K. J. Millman, N. Mayorov, A. R. J. Nelson, E. Jones, R. Kern, E. Larson, C. J. Carey, İ. Polat, Y. Feng, E. W. Moore, J. VanderPlas, D. Laxalde, J. Perktold, R. Cimrman, I. Henriksen, E. A. Quintero, C. R. Harris, A. M. Archibald, A. H. Ribeiro, F. Pedregosa, P. van Mulbregt, and SciPy 1.0 Contributors, Nature Methods **17**, 261 (2020).
[51] E. Hairer and G. Wanner, *Solving Ordinary Differential Equations II. Stiff and Differential-Algebraic Problems*, Vol. 14 (Springer, New York, 1996).
[52] R. J. Luyken, A. Lorke, A. O. Govorov, J. P. Kotthaus, G. Medeiros-Ribeiro, and P. Petroff, Appl. Phys. Lett. **74**, 2486 (1999).
[53] J. R. Norris, in *Markov Chains*, Cambridge Series in Statistical and Probabilistic Mathematics (Cambridge University Press, Cambridge, 1997), pp. 60–107.
[54] A. A. Markov, Sci. Context **19**, 591 (2006).
[55] J. W. Eaton, D. Bateman, S. Hauberg, and R. Wehbring, GNU Octave version 5.2.0 manual: A high-level interactive language for numerical computations (2020).
[56] See Supplemental Material at http://link.aps.org/supplemental/10.1103/PhysRevB.104.205310 for simulations under additional initial conditions.